Remote Sensing of Environment 283 (2022) 113311

Contents lists available at ScienceDirect

Remote Sensing of Environment

journal homepage: www.elsevier.com/locate/rse

Development of a filter-based near-surface remote sensing system to retrieve far-red sun-induced chlorophyll fluorescence

Jongmin Kim [a], Youngryel Ryu [a,b,c,*], Benjamin Dechant [c,d,e]

[a] Interdisciplinary Program in Landscape Architecture, Seoul National University, Seoul, South Korea
[b] Department of Landscape Architecture and Rural Systems Engineering, Seoul National University, Seoul, South Korea
[c] Research Institute for Agriculture and Life Sciences, Seoul National University, Seoul, South Korea
[d] German Centre for Integrative Biodiversity Research (iDiv) Halle-Jena-Leipzig, Leipzig, Germany
[e] Leipzig University, Leipzig, Germany

ARTICLE INFO

Edited by Jing M. Chen

Keywords:
Sun-induced chlorophyll fluorescence
Photodiode
Bandpass filters
Spectroradiometer

ABSTRACT

Observations of sun-induced chlorophyll fluorescence (SIF) by remote sensing have improved our understanding of the structural and physiological dynamics of vegetation. Substantial efforts have been made to measure SIF with ground-based sensing systems, but field observation data for various plant functional types are still sparse. This is partly due to the limited availability of commercial SIF measurement systems, the relatively high cost of hyperspectral spectroradiometers, and the difficulties of sensor calibration and maintenance in the field. We developed a filter-based smart near-surface remote sensing system for SIF (4S-SIF) to overcome the technical challenges of monitoring SIF in the field, which also decreased the sensor cost, thus enabling more comprehensive spatial sampling. To retrieve SIF, we combined ultra-narrow bandpass filters (full width half maximum $<$1.3 nm) and photodiode detectors to observe electromagnetic radiation at specific wavelengths (757, 761, and 770 nm). We confirmed that the spectral and radiometric performance of the bandpass filters was satisfactory to retrieve SIF by comparing them to a high-spectral-resolution spectroradiometer that served as a reference. In particular, we confirmed that the digital numbers (DNs) from 4S-SIF exhibited linear relationships with the DN from the reference spectroradiometer in each band ($R^2 > 0.99$). In addition, we developed equations to correct for temperature-induced changes in filter transmittance, such that SIF can be reliably extracted in outdoor environments without the need to actively stabilize the temperature. Furthermore, we confirmed that the SIF signal from 4S-SIF had a strong linear relationship with the reference spectroradiometer-based SIF. Importantly, this relationship held even when the physiological mechanisms of the plant were altered by a herbicide treatment that induced substantial changes in the SIF signal ($R^2 = 0.85$, relative RMSE = 0.22), which indicated that 4S-SIF could be used to retrieve SIF. We believe that 4S-SIF will be a useful tool for collecting in-situ SIF data across multiple spatial and temporal scales.

1. Introduction

Recent advances in satellite remote sensing of sun-induced chlorophyll fluorescence (SIF) provide us with new opportunities to understand the structural and physiological dynamics of vegetation from regional to global scales (Frankenberg and Berry, 2018; Ryu et al., 2019). Remotely sensed SIF has enhanced our ability to estimate gross primary production (GPP) because of the strong relationship between SIF and GPP (Frankenberg et al., 2011; Joiner et al., 2013; Joiner et al., 2014; Li and Xiao, 2022; Sun et al., 2018; Sun et al., 2017; Zhang et al., 2016). Satellite-based SIF has also been used as a proxy for vegetation phenology (Jeong et al., 2017; Lu et al., 2018; Walther et al., 2016), and as an indicator of drought stress in tropical rainforest and evergreen needle leaf forest (Yang et al., 2018a; Zuromski et al., 2018) and has been used to improve large-scale estimates of carbon, water, and energy fluxes (e.g., Alemohammad et al. (2017).

Despite the progress made in satellite SIF retrieval and the promising applications, the complex relationship between SIF and GPP is not fully understood. While SIF has a stronger linear relationship with absorbed photosynthetically active radiation (APAR) than GPP in unstressed soybean and rice (Miao et al., 2018; Yang et al., 2018b) and stressed sugar beet (Wieneke et al., 2018a), other studies have reported weaker

* Corresponding author at: Department of Landscape Architecture and Rural Systems Engineering, Seoul National University, Seoul 151-921, South Korea.
E-mail address: yryu@snu.ac.kr (Y. Ryu).

https://doi.org/10.1016/j.rse.2022.113311
Received 15 July 2022; Received in revised form 1 October 2022; Accepted 11 October 2022
Available online 20 October 2022

and more non-linear relationships between SIF and GPP. For example, the correlation between SIF and GPP was reported to be weak in evergreen needle leaf forest, cornfield, cropland, and mixed forest because environmental conditions affected the SIF-GPP relationships (Cheng et al., 2013; Nichol et al., 2019; Paul-Limoges et al., 2018). It was also found that SIF was less responsive to drought than GPP in a Mediterranean pine forest (Wohlfahrt et al., 2018), and the relationships with GPP in other ecosystems were also reported to be complex (Martini et al., 2022; Wieneke et al., 2018a). Some studies have shown that the canopy-level SIF-GPP relationship is non-linear in evergreen needle leaf forest and maize (Kim et al., 2021; Liu et al., 2021; Pierrat et al., 2022; Yang et al., 2022). While considerable progress has been made in disentangling canopy structural and physiological components in SIF (Dechant et al., 2022; Dechant et al., 2020; Kim et al., 2021; Xu et al., 2021; Zeng et al., 2019), more research using ground-based SIF is required to evaluate and better understand satellite-based SIF and its relationship with GPP.

Numerous studies have developed systems to monitor ground-based SIF based on hyperspectral spectroradiometers. These systems typically consist of commercially available hyperspectral spectroradiometers and other components assembled in different ways. For example, there are SFLUOR box, Fluospec, FAME, PhotoSpec, FloX, TriFLEX, and SIFspec systems (Campbell et al., 2019; Cogliati et al., 2015; Daumard et al., 2010; Du et al., 2019; Goulas et al., 2017; Grossmann et al., 2018; Gu et al., 2019; Yang et al., 2018c). The major differences between these systems are what kind of devices and techniques were used to measure both reflected light from vegetation and incoming solar irradiance or how to control the environmental conditions within the system box to guarantee stability of spectroradiometer measurements. The FloX system (JB Hyperspectral Devices, Düsseldorf, Germany) is a commercialized version of a system initially developed by researchers using similar components to those used in other, custom-made systems. It has been widely applied for a variety of research purposes (Dechant et al., 2022; Martini et al., 2022; Migliavacca et al., 2017). Although not configured as a system, numerous efforts have been made to observe ground-based SIF using commercial hyperspectral spectroradiometers (Cheng et al., 2013; Damm et al., 2010; Julitta et al., 2016; Liu and Liu, 2018; Meroni and Colombo, 2006; Rossini et al., 2010; Wieneke et al., 2018b; Zhou et al., 2016).

Although numerous efforts have been made to monitor ground-based SIF, there are three major limitations of spectroradiometer-based SIF sensing systems. The first limitation is that commercially available hyperspectral spectroradiometers are expensive, which has obvious implications regarding the feasibility of their installation at multiple sites (Kim et al., 2019; Richardson et al., 2009; Ryu et al., 2010). Second, spectroradiometer-based systems are challenging to use in practice in order to meet the strict requirements necessary for high-quality SIF retrieval. Spectroradiometers can be influenced by environmental factors such as air temperature and humidity, which is difficult to control in the field (Pacheco-Labrador and Martín, 2015; Wang et al., 2015). In particular, uncontrolled temperatures can trigger changes in radiometric magnitude, the signal to noise ratio, and spectral features (Hueni and Bialek, 2017; Pacheco-Labrador et al., 2019). Alterations of spectroradiometer performance caused by temperature lead to uncertainties in SIF retrieval (Damm et al., 2011). In addition, condensation can occur if the temperature inside the system housing is below the dew point and the housing is not actively dried because active temperature control of hyperspectral systems is typically conducted at low temperatures to reduce the influence of dark current in the signal (Yang et al., 2018c). Active temperature and humidity control in humid locations is, therefore, necessary to obtain reliable measurements (Kim et al., 2021; Magney et al., 2019). However, this adds to the cost and complexity of optical systems. Third, hyperspectral spectroradiometers are difficult to use for non-experts, which is an important issue because many users may have a background in eddy covariance measurements, ecology, plant physiology, or geography, but not optical spectroscopy. To obtain more observations in various regions and ecosystems, the observing system needs to be easy to use. Thus, a relatively inexpensive ground-based SIF system that is insensitive to environmental conditions and easy to handle in the field is needed.

For vegetation monitoring, spectroradiometers can be replaced with systems that combine photodiodes and optical filters if only specific wavelengths are needed. For example, variation in plant leaf physiology can be estimated from the observed reflectance in only a few wavelength bands, i.e., the photochemical reflectance index (PRI) (Gamon et al., 1997). To select the desired wavelength band, multi-spectral sensor systems combining photodiodes and filters have been developed (Garrity et al., 2010; Pontailler et al., 2003; Pontailler and Genty, 1996). These systems have been used to monitor vegetation, including deciduous and evergreen trees and crop species, and have been proven to operate robustly over long periods of time (Baldocchi et al., 2020; Gamon et al., 2015; Magney et al., 2016; Soudani et al., 2012). The combination of photodiodes and filters has potential to be used to extract SIF more easily as the Fraunhofer line depth (FLD) method can extract SIF using only two or three spectral bands, inside and outside of the O_2A band (Meroni et al., 2009; Plascyk, 1975). In other words, SIF can be extracted by observing only a few specific spectrally narrow wavelength bands (e.g., 757 and 760.7 nm). Although several previous studies have combined filters and photodiodes to extract SIF at the leaf scale (Kebabian et al., 1999; Louis et al., 2005; Moya et al., 2004), a system for continuously monitoring canopy-level SIF in the field has not yet been devised. Furthermore, the previous studies did not directly test if the developed system could reliably retrieve SIF with dedicated experiments that can considerably change the fluorescence yield during relatively short periods of time. Such experiments include treating plants with herbicides such as 3-(3′,4′-dichlorophenyl)-1, 1-dimethylurea (DCMU) (Pinto et al., 2020; Rossini et al., 2015), or suddenly exposing dark-adapted vegetation to strong light (Grossmann et al., 2018; Zeng et al., 2022), i.e. making use of the Kautsky effect, or controlling the amount of light emitted from the surface with light emitting diode (LED) with a similar spectral shape as SIF (Burkart et al., 2015). Therefore, further experiments should be conducted to confirm the reliability of the retrieved SIF.

Here, we present filter-based smart near-surface remote sensing system for SIF (4S-SIF) to overcome the technical challenges of monitoring SIF in the field as well as to decrease sensor cost for more comprehensive spatial sampling. To monitor SIF, we combined ultra-narrow bandpass filters and photodiode detectors to observe electromagnetic radiation at specific wavelengths. This paper consists of three main parts:

1) Description of the developed 4S-SIF.

2) Evaluation of 4S-SIF using a commercial hyperspectral spectroradiometer as a reference.

3) Evaluation of the SIF retrieval quality of 4S-SIF by comparison with reference instruments in a realistic field scenario under rapidly changing SIF levels induced by DCMU treatment.

Because the main purpose of this study was sensor development, we have included the interpretations of the results in the Materials and methods section.

2. Materials and methods

2.1. Instrument design and technical specifications

The fundamental structure of 4S-SIF was based on a previous instrument (4S) designed to measure multi-spectral reflectance (Fig. S1 and Kim et al. (2019). 4S-SIF consisted of a Raspberry pi microcomputer (Raspberry Pi b3 module; Raspberry Pi Foundation, UK), customized 3D-printed structure, photosensor amplifier (C9329; Hamamatsu Photonics, Japan), internet router, silicon photodiode (S2386-18 K; Hamamatsu Photonics), and three ultra-narrow bandpass filters (Fig. 1). A list of all of the components of the 4S-SIF sensor, together with their price and

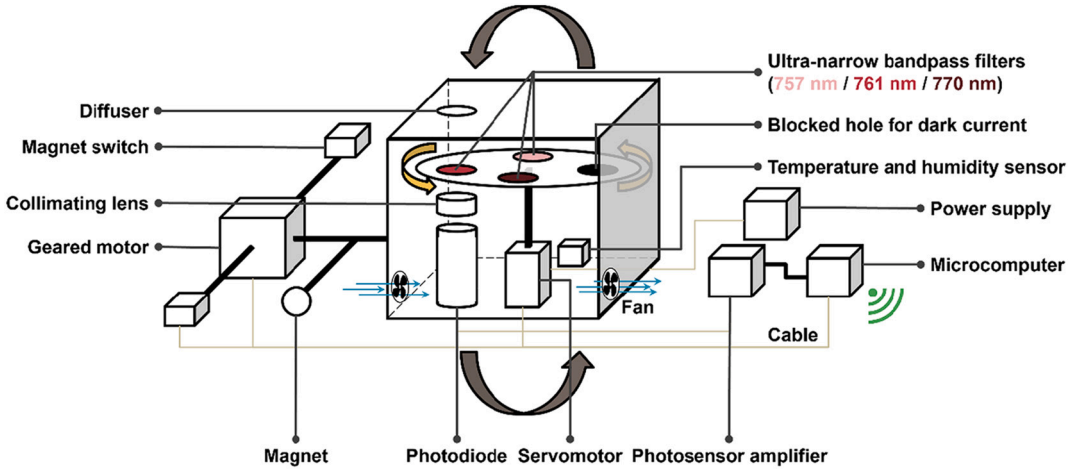

Fig. 1. Schematic of Smart Surface Sensing System for SIF.

manufacturer, is given in Appendix. A. Regarding the sensor housing parts, we made a hole in a customized 3D-printed structure and covered it with white diffusing glass (White diffusing glass with 25 mm diameter; Edmund Optics). We observed upward and downward irradiance by rotating one sensor using a geared motor. The details of how bi-hemispherical irradiance was measured are presented in section 2.6.2. Three of the slots were used for ultra-narrow bandpass filters, to collect light for each specific wavelength respectively (757, 761, and 770 nm; 25 mm diameter). The selected three spectral bands are located inside and outside of the O_2A band and they can be used for SIF retrieval as we described in the introduction. The performance of the ultra-narrow bandpass filters is described in section 2.2. In the case of the 761 nm filter, a second bandpass filter that only transmitted light in the spectral range from 710 to 780 nm (745BP70 with 25 mm diameter.; Omega Optics;) was added to minimize the amount of transmitted light outside the desired wavelength band. This was because the light intensity in the O_2A band (760.7 nm) was lower than in the other bands, and one ultra-narrow bandpass filter (optical density = 4) could not sufficiently block the light outside the 710–780 nm range. The optical density was defined as the ratio of the intensity of light falling on the bandpass filter to that of the light transmitted through the filter (Zhang and Hoshino, 2019). The fourth slot was blocked to measure the dark current. The wheel was combined with a servomotor (PDI-6225MG-300; Digital Servo, China). As the servomotor rotated the wheel, a single photodiode measured the light passing through three different ultra-narrow bandpass filters, as well as the dark current. We installed a collimating lens between the ultra-narrow bandpass filter and photodiode (LA1540-ML; Thorlabs, USA) to increase the number of photons reaching the photodiode, and to ensure that only photons that hit the ultra-narrow bandpass filter orthogonally to its surface were measured. This was because changes in the angle of incidence can cause considerable wavelength shifts during the transmittance of the bandpass filters (Fig. S2) (Renhorn et al., 2016; Rienstra, 1998). The customized 3D-printed structure was made of polyethylene terephthalate (PET) to minimize structural changes in the outdoor environment, and it supported the diffuser, ultra-bandpass filters, and collimating lens for outdoor use. We also installed two fans (DC brushless fan; Jameco Electronics, USA) to circulate the air inside and outside the sensor. One fan pulled outside air into the sensor and the other removed the internal air from the sensor (Fig. 1 and please check Fig. S1). We placed a 3D printed cap with holes on the fans to prevent outside light from penetrating through the holes in the fan with a space between cap and the holes for air circulation. We also installed a sensor to measure temperature and humidity (DHT22; Adafruit, USA) in the 4S-SIF box and connected it to a microcomputer to save the data.

To quantify the electromagnetic radiation at specific wavelengths, we connected the photodiode to a photosensor amplifier. When the silicon photodiode captured a photon, a signal was formed and then amplified by the photosensor amplifier. The photosensor amplifier converted the analog signal into a digital number (DN). We collected the DN values and saved them as text files in the microcomputer. We developed a custom Python (Python Software Foundation, USA) script that ran on the microcomputer to automatically control the workflow chain. The stored data were downloaded from the internet. The cost of 4S-SIF was around US$4300 (Appendix A) as of July 2021 in South Korea. We uploaded information about codes, 3D printing, and components information (e.g., the photosensitivity curve of 4S-SIF photodiode) to our GitHub repository (https://kimhyodong.com/github/).

2.2. *Performance of the ultra-narrow bandpass filters*

Accurate specification of a customized ultra-narrow bandpass filter is one of the key factors influencing the extraction of SIF using the FLD method (Damm et al., 2011; Meroni et al., 2009). To verify the performance of the ultra-narrow bandpass filters, we used a light source (HL-2000-CAL; Ocean Insight, USA) and hyperspectral spectroradiometer (QE Pro; Ocean Insight). The QE Pro hyperspectral spectroradiometer covers a spectral range of 730–790 nm, with a resolution of 0.17 nm and sampling interval of 0.07 nm. In this study, we defined the QE Pro hyperspectral spectroradiometer as the reference spectroradiometer. We aligned the light source, diffuser, ultra-narrow bandpass filters, and collimating lens, and used a fiber to connect them to the reference spectroradiometer in a dark room (Fig. S3). We then measured the ultra-narrow bandpass filter transmittance by calculating the ratio of observed light with and without the ultra-narrow bandpass filters. The ultra-narrow bandpass filters exhibited around 1 nm full width half maximum (FWHM) and the peak sensitivity were 757.7, 760.6, and 770 nm, respectively (Fig. 2). For the sake of convenience, we referred to the filters in terms of their center wavelength. In addition, we tested whether the entire 4S-SIF sensor (i.e., including the housing and diffuser material) responded at the same wavelength as the observed ultra-narrow bandpass filter transmittance. We irradiated the 4S-SIF with monochromatic light at 1-nm intervals using a single monochromator (TMc300; Bentham, UK) in a dark room. Although the spectral resolution of the monochromator was 1 nm, the entire 4S-SIF sensor response was consistent with the observed filter transmittance (Fig. S4).

Furthermore, we used simulations to verify that the observed filter transmittances were sufficient to retrieve SIF as follows. First, we used in-situ observed incoming irradiance spectral data from the reference spectroradiometer (data from (Kim et al., 2021). Second, we computed the outgoing irradiance data by multiplying the incoming spectral data by the reflectance. We simulated the reflectance using the PROSAIL model (Jacquemoud and Baret, 1990; Jacquemoud et al., 2009; Verhoef,

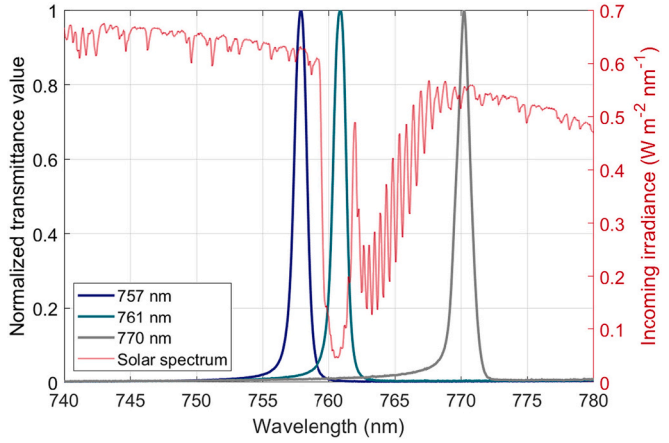

Fig. 2. Normalized transmittance from ultra-narrow bandpass filters and incoming solar irradiance observed by the reference spectroradiometer. The center wavelengths of each ultra-narrow bandpass filter are given in the legend.

1984). Third, we added the simulated spectral curve of chlorophyll fluorescence obtained using the Soil Canopy Observation of Photosynthesis and Energy (SCOPE) model (Van der Tol et al., 2014; Van der Tol et al., 2009; Vilfan et al., 2016) to the simulated reflected light. A detailed explanation of the input parameters of PROSAIL and SCOPE is provided in the Supplementary Materials (Fig. S5 and Table S1). Fourth, we obtained the photosensitivity data per wavelength of the photodiode from the manufacturer and multiplied it with the incoming and outgoing irradiance. Finally, we extracted SIF using the 3FLD method with three bands (Damm et al., 2011; Meroni et al., 2009; Mohammed et al., 2019; Plascyk, 1975). In the 3FLD method, we selected one spectral window for "in" for the O_2A band and two spectral windows for "out" for the up- and down-welling irradiance. Eqs. 1 and 2 give the SIF retrieval for the 3FLD method.

$$SIF = \frac{L_{O2A} - \frac{E_{O2A}}{(W_l \times E_l - W_r \times E_r)} \times \left(W_l \times L_l + W_r \times L_r\right)}{1 - \frac{E_{O2A}}{(W_l \times E_l + W_r \times E_r)}}, \text{where} \quad (1)$$

$$W_l = \frac{\lambda_{O2A} - \lambda_l}{\lambda_r - \lambda_l}, \text{and } W_r = \frac{\lambda_r - \lambda_{O2A}}{\lambda_r - \lambda_l} \quad (2)$$

where L_{O2A} and E_{O2A} represent the up-welling irradiance from vegetation and down-welling irradiance from the sky in the O_2-A region, respectively. For the O_2-A region in the filter transmittance-based 3FLD method ($3FLD_{trans\ applied}$), we used transmitted irradiance from the 761 nm filter. L_l and L_r represent the up-welling irradiance from vegetation through the 757 and 770 nm filters. E_l and E_r represent the down-welling irradiance from the sky through the 757 and 770 nm filters. λ_{O2A} is the center wavelength of the 761 nm filter. λ_r And $\lambda_l$represent the center wavelengths of the 770 and 757 nm filters, respectively. For 3FLD with the one-pixel method ($3FLD_{one\ pixel}$), we did not use filter transmittance. We used 758.5 and 770.5 nm for "out", and 760.5 nm for "in", for the O_2A band in the spectral data from the reference spectroradiometer. We averaged two neighboring detector pixels to reduce noise. To verify the simulation cases, we randomly selected 1 of the 100 samples each for incoming irradiance, reflectance, and chlorophyll fluorescence, and then extracted SIF. This method was repeated 10,000 times.

After extracting SIF using $3FLD_{trans\ applied}$, we corrected the magnitude of extracted SIF (Appendix. B). We found that the SIF extracted using $3FLD_{trans\ applied}$ was lower than that extracted from $3FLD_{one\ pixel}$. The extracted SIF using a wider wavelengths range could show a different magnitude compared to extracted SIF from $3FLD_{one\ pixel}$ (Belwalkar et al., 2022; Nakashima et al., 2021). We obtained the equation for the relationship between extracted SIF from $3FLD_{trans\ applied}$ and $3FLD_{one\ pixel}$ using a linear regression model, and then used it to correct the magnitude.

The relationship between $3FLD_{trans\ applied}$ and input SIF (chlorophyll fluorescence value at 760 nm) was linear although the R^2 value was lower, and the relative root mean square error (rRMSE) was higher for $3FLD_{trans\ applied}$ than for $3FLD_{one\ pixel}$ (Fig. 3). This result indicates that $3FLD_{trans\ applied}$ can be used to SIF retrieval. We discussed the more detailed aspects of the relationship between $3FLD_{trans\ applied}$ than for $3FLD_{one\ pixel}$ in discussion section 4.4.

2.3. Performance of the 4S-SIF diffuser

To test for consistency of the cosine responses among the three ultra-narrow bandpass spectral filters equipped with the diffuser, we compared the relative response of light intensity from three ultra narrow bandpass filters using a theoretically ideal cosine curve (Fig. 4). We used a customized goniometer (Ryan, Korea) to control the light source zenith angle. We used a halogen light source (LS-F100HS-IR; Light Bank, Korea) and varied its zenith angle from 0 to 90° with a 10° interval. We then measured the transmitted light corresponding to the three ultra-narrow bandpass filters of the 4S-SIF by rotating the wheel to which the filters were attached. The experiment was conducted in a dark room. The differences between the relative responses of the 757, 761, and 770 nm filters and ideal cosine curve were 1.1%, 1.4%, and 1.8%, respectively, within 60° of the light source zenith angle, and 28%, 32%, and 20%, respectively, within 70° of the light source zenith angle (Fig. 4).

2.4. Radiometric calibration

We used a reference spectroradiometer to radiometrically calibrate the 4S-SIF, because we did not have a light source or integrating sphere that fit the 4S-SIF diffuser. Radiometric calibration of the reference spectroradiometer was done using a HL-2000-CAL light source (Ocean Insight). For cross-calibration using sunlight under clear sky conditions (DOY 285, 2021), we installed both sensors on the rooftop of a building at Seoul National University (SNU), Seoul, Korea. The 4S-SIF and tip of the fiber connected to the reference spectroradiometer were installed facing the zenith. We compared the voltages produced by the silicon photodiode of the 4S-SIF to the spectral irradiance observed from the reference spectroradiometer across a wide range of radiation intensities. To minimize the influence of external environmental factors (e.g., temperature and humidity), the reference spectroradiometer was kept in a temperature-controlled enclosure (EIC Solutions Inc., USA) at 20 °C. To match the spectral resolution between the reference spectroradiometer and 4S-SIF, we applied the transmittance curves of the ultra-narrow bandpass filters to the spectral data obtained by the reference spectroradiometer. In addition, we accounted for the photosensitivity curve of the 4S-SIF photodiode to the spectral data from the reference spectroradiometer for more accurate radiometric calibration. The DN from the 4S-SIF had a very strong linear relationship with the spectral irradiance values from the reference spectroradiometer ($R^2 > 0.98$ for all bands, Fig. 5). During cross-calibration, we did not control the temperature for 4S-SIF. We only corrected wavelength shifts over the temperature in ultra-narrow bandpass filters. We described the correction method next chapter 2.5.

2.5. Temperature response of the 4S-SIF

To test the stability of the ultra-bandpass filters under realistic outdoor environmental conditions, we exposed them to various temperatures. We placed the ultra-narrow bandpass filters, light source, and HMP 155 temperature probe (Vaisala, Finland) inside a temperature control box (EIC Solutions Inc.) and then varied the temperature from 15 °C to 45 °C at intervals of 0.2 °C. We installed the reference spectroradiometer outside the temperature control box at room temperature, and placed only the tip of the fiber into the temperature control box to observe the transmitted light passing through the ultra-narrow bandpass

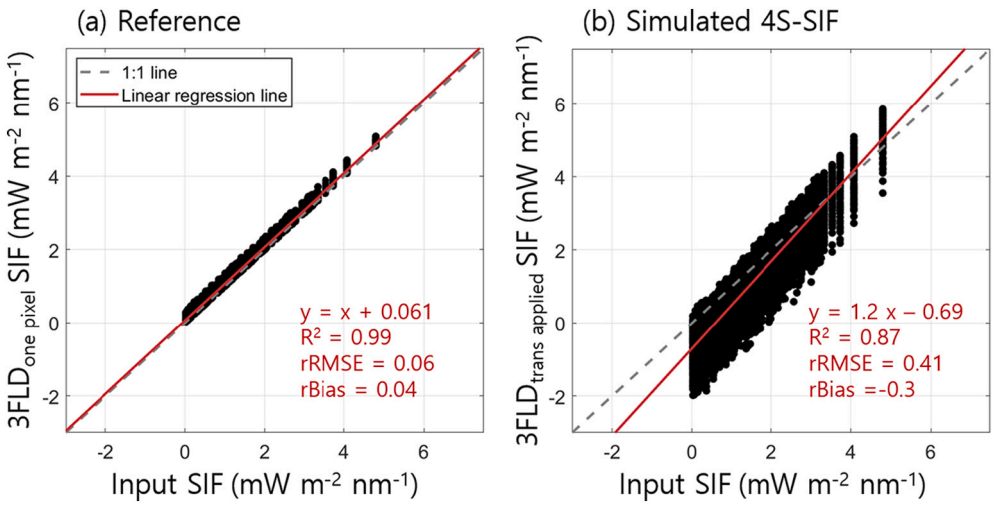

Fig. 3. Comparison of simulated SIF retrieval between the reference spectroradiometer (a) and simulated 4S-SIF sensor (b). $3FLD_{one\ pixel}$ is a one pixel-based 3FLD method and $3FLD_{trans\ applied}$ is an applied filter transmittance-based 3FLD method. Input SIF indicates a value corresponding to a wavelength of 760 nm for chlorophyll fluorescence and was used as input data in the simulation. We used various reflectance, chlorophyll fluorescence, and irradiance values in the simulation.

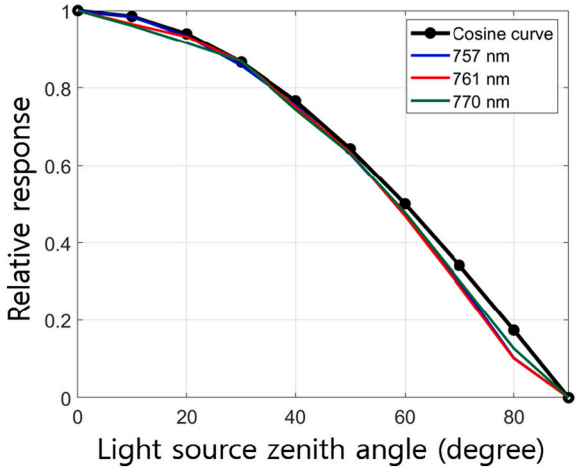

Fig. 4. Relative response of three ultra-narrow bandpass filters: comparison with an ideal cosine curve. The wavelengths in the legend correspond to the peak transmittance of the ultra-narrow bandpass filters.

filter under conditions in which the temperature changed continuously. We measured the temperature and transmitted spectral data every minute. The peak and overall transmittance curve tended to shift toward longer wavelengths as the temperature increased (Fig. 6). In addition, the transmittance from the 770 nm filter had much higher sensitivity to temperature than the other two ultra-narrow bandpass filters. Because it was manufactured by a different company, it is possible that the 770 nm filter was comprised of different materials than the 757 and 761 nm filters (Appendix A).

We then tested whether the temperature-induced transmittance changes of the ultra-narrow bandpass filters affected SIF retrieval. To simulate the effect of temperature on filter transmittance, we used the observed spectral data (incoming irradiance and chlorophyll fluorescence) and temperature-induced transmittance changes. First, we used in-situ irradiance spectral data from the reference spectroradiometer for radiometric calibration. Second, we multiplied the incoming spectral data by the reflectance data to determine the outgoing irradiance without chlorophyll fluorescence. We assumed that the reflectance value was 0.5, and that the reflectance was constant regardless of the wavelength, which removed the reflectance shape effect and quantified only the temperature-induced transmittance changes of the ultra-narrow bandpass filters. Third, we added the in-situ spectral curve of chlorophyll fluorescence to the simulated reflected light (data from (Yang

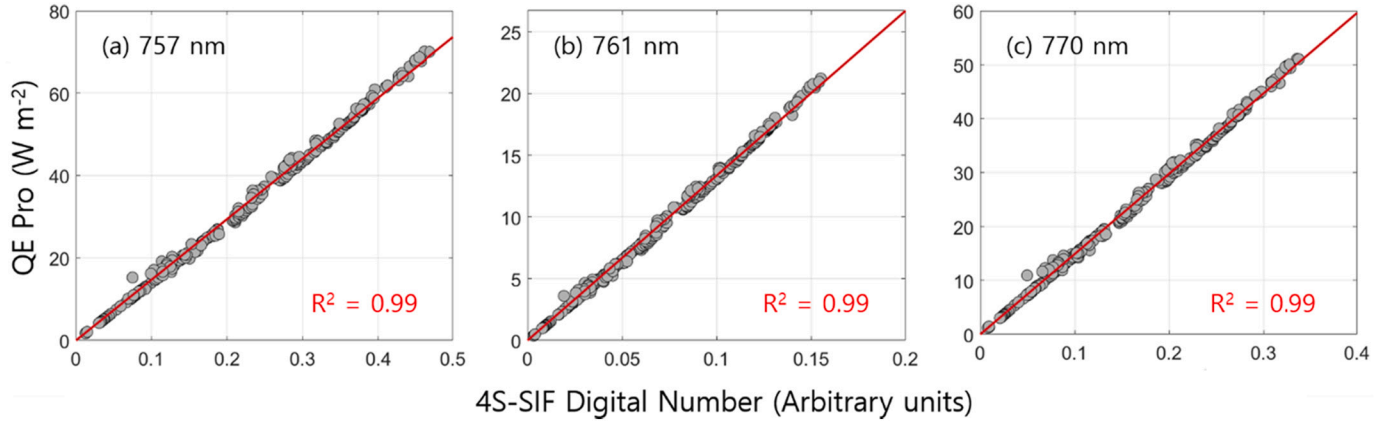

Fig. 5. Relationships between the irradiance from the reference spectroradiometer and digital number (DN) for the 4S-SIF. The red line is the result of linear regression. The wavelengths shown in (a)–(c) correspond to the peak transmittance of each ultra-narrow bandpass filter. (For interpretation of the references to colour in this figure legend, the reader is referred to the web version of this article.)

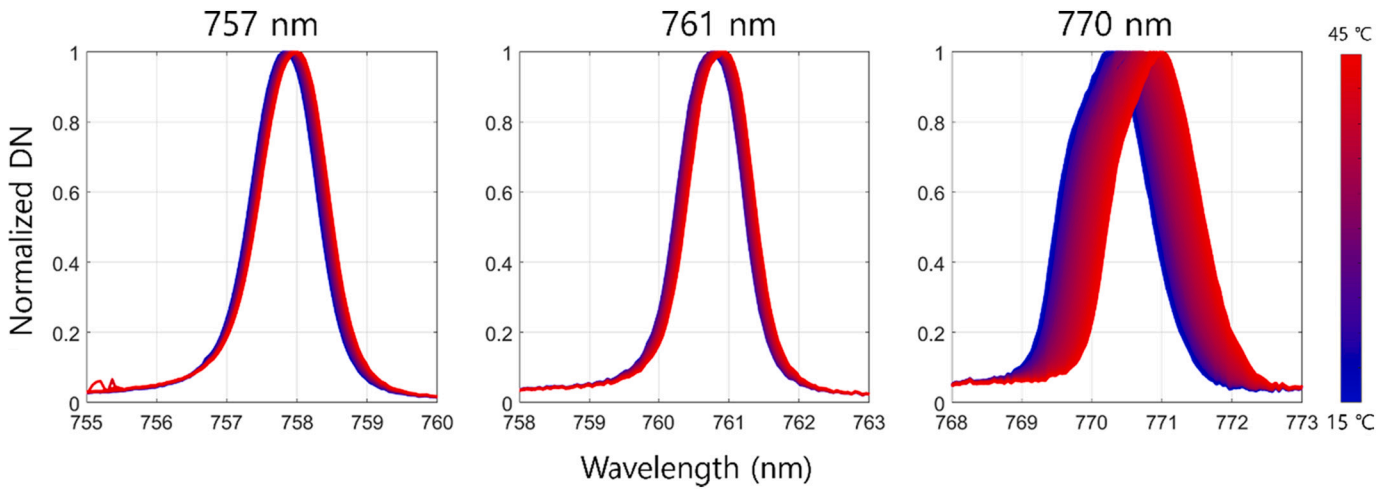

Fig. 6. Temperature response of the ultra-narrow bandpass filters. The wavelengths shown in (a)–(c) correspond to the peak transmittance of each ultra-narrow bandpass filter.

et al., 2018b)). Fourth, we multiplied the photosensitivity of the photodiode with incoming and outgoing irradiance. We used the photosensitivity data provided by the manufacturer. Fifth, we applied the temperature dependent ultra-narrow bandpass filter transmittance from the temperature sensitivity experiment to the incoming and outgoing irradiance spectral data processed as described above (Fig. 6). Finally, we extracted SIF using the 3FLD method with three bands, based on Eqs. 1 and 2.

The simulated SIF decreased with increasing temperature (Fig. 7). We fitted the relationship between the simulated SIF and temperature, and used the regression equation obtained through this simulation to correct the estimated SIF in the outdoor experiment. The simulated SIF was strongly correlated with temperature (Fig. 7, $R^2 = 0.95$). We used the equation from the linear regression model to correct the temperature effect on SIF retrieval in outdoor measurements, as reported in section 2.6.3.

2.6. Evaluation of the 4S-SIF sensor in an outdoor SIF retrieval experiment

2.6.1. Overview of the outdoor experiment

We investigated whether 4S-SIF could detect SIF emitted from plants

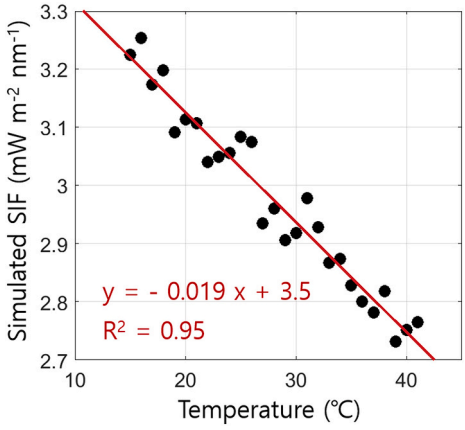

Fig. 7. Response of the simulated SIF to temperature. The SIF simulation was based on observed solar irradiance data and the fixed reflectance, and the temperature response was driven by the changes in optical properties of ultra-narrow bandpass filters. The red line is the result of linear regression. (For interpretation of the references to colour in this figure legend, the reader is referred to the web version of this article.)

in an outdoor environment (Fig. S6). The experimental site was a building rooftop at SNU. We transplanted strawberry (*Fragaria* × *ananassa*, Duchesne, Rosaceae) over an area of 1.8 × 1.8 m, with a bedding depth of about 0.4 m in a mixed organic and pearlite soil (Lee et al., 2015). This small plot was built in open space to avoid shading from canopies and buildings. We conducted the experiment from DOY 285 to 295 in 2021. We planted the strawberry plants before October, and irrigated them with around 7 L of water every morning.

We installed the reference spectroradiometer and 4S-SIF on horizontal booms 0.8 m above the strawberry canopy (Fig. S6). In the reference spectroradiometer, we used a custom-made rotating prism system, i.e., a servomotor combined with a prism, to measure up- and down-welling irradiance using one optical fiber and a spectroradiometer (Kim et al., 2021). We changed the orientation of the prism at regular intervals using a servomotor, to observe the up- and down welling irradiance of a single fiber with one spectroradiometer. The integration time of the reference spectroradiometer was set to 0.3 s in the upward direction and 0.9 s in the downward direction. We observed an up- and down-welling irradiance signal once within 1 min. To avoid mixing the up- and down-welling signals, a sufficient waiting time (10 s) between two observations was used. We kept the reference spectroradiometer in a temperature-controlled enclosure (EIC Solutions) at 20 °C because variations in temperature and humidity could influence the performance of the charge-coupled device (CCD) array in the reference spectroradiometer. We calculated the radiometric footprint by applying a method reported by Marcolla and Cescatti (2018). The footprint was estimated from the nadir view angle and distance from the sensor to the top of the canopy. >50% of the signals of both sensors were driven by the strawberry canopy.

2.6.2. Data collection and filtering in 4S-SIF

To measure the up- and down-welling irradiance signals from 4S-SIF, we combined the sensor with a geared motor (Fig. 1). We used a magnetic switch to accurately control the position of the sensor in the upward and downward directions. We attached the magnet at the point where the motor and sensor were connected, installed the magnet switch, and operated it at 0 and 180° above the ground. When the magnet was rotated by the geared motor (DC 12 V, 3000 rpm; GGM, South Korea) and was near the magnetic switch, the read switch inside the magnetic switch was turned on and a current was generated. When the microcomputer recognized the current flow, we stopped the geared motor from moving. The geared motor could therefore be used to control the sensor orientation at 0 and 180°, to measure up- and down-welling irradiance, respectively (Fig. S7). We confirmed that the sensor was

orientated correctly using a bubble level every morning and evening.

Approximately 40 data points per each ultra-narrow bandpass filter were stored in 1 min interval. In order to remove the observed data when the servomotor is rotating, we only selected the points observed after the motor stopped. Using the selected points, we constructed a histogram and calculated a standard deviation. Then, we further selected the values within ±20% standard deviation of the peak count in the histogram. For 1 min, >40 points data corresponding to three ultra-narrow filters and one dark current were chosen in the up- and down-welling directions. In addition, to remove extreme outliers from averaged 1 min data, we used additional outlier filter (Hampel, 1974). The outlier filter uses the median absolute deviation and standard deviation within a given time window. We applied a three standard deviations criterion and window length of 30 data points. We used the *'hampel'* function in MATLAB (MathWorks Inc., USA). Most of the severe outliers occurred on cloudy days when the sky conditions changed abruptly between the up- and down-welling irradiance observations.

2.6.3. Retrieval of the SIF and vegetation index

We used the 3FLD method to extract SIF from the reference spectroradiometer and 4S-SIF (Eqs. 1 and 2). To extract three bands from the spectral data obtained by the reference spectroradiometer, we applied the transmitted spectral data from each ultra-narrow filter observed at 25 °C to the observed incoming and outgoing irradiance. In addition, we multiplied the photosensitivity values of the photodiode with the observed incoming and outgoing irradiance from in-situ measurement. For the 4S-SIF, we used the values corresponding to the three filters as the three bands. We calculated SIF using the radiometrically calibrated value (magnitude correction; see section 2.4). We corrected the temperature effect of the extracted SIF using the equation presented in section 2.5. We measured the air temperature near the ultra-narrow bandpass filter and used it for the temperature correction (Fig. 1). The SIF estimated from the 4S-SIF was also corrected to a value corresponding to 25 °C, as for the reference spectroradiometer. To reduce random noise, we averaged the observed spectral data within 1 min or 30 min intervals and then applied the 3FLD method to extract SIF (Zarco-Tejada et al., 2018). In addition, we corrected the magnitude of SIF from the 4S-SIF (section 2.2). We used the linear regression equation for the relationship between SIF from $3FLD_{\text{trans applied}}$ and $3FLD_{\text{one pixel}}$ to correct the magnitude of SIF $3FLD_{\text{trans applied}}$ (Appendix B).

To determine the effect of changes in chlorophyll fluorescence on canopy-level SIF, we estimated SIF yield as follows:

$$SIF\ yield = \frac{SIF}{NIR_v \times PAR} \tag{3}$$

where NIR_V is the product of the normalized difference vegetation index (NDVI) ×near-infrared (NIR) reflectance (Badgley et al., 2017), and PAR is photosynthetically active radiation. SIF is an optical signal in the NIR region, where photons can be strongly scattered in vegetation canopies (Yang and van der Tol, 2018). Therefore, the SIF observed in the signal at the top of the canopy was influenced by the canopy escape fraction (f_{esc}), which is the fraction of SIF photons emitted from all leaves that escape from the canopy (Yang et al., 2020; Zeng et al., 2019). f_{esc} can be robustly estimated as $\frac{NIR_v}{fPAR}$ (Zeng et al., 2019). *fPAR* is the fraction of PAR absorbed by the canopy. The observed SIF can be written as APAR × Φ_F × f_{esc} (Dechant et al., 2020). Φ_F is chlorophyll fluorescence yield (SIF yield) and the APAR is absorbed PAR and it is the product of *fPAR* × PAR. Therefore, when the above formulae are rearranged, f*PAR* can be cancelled out, resulting in Eq. 3 for the SIF yield.

The PAR and NDVI were measured using a quantum sensor (LI-190; LI-COR, USA) and four band spectral sensors (4S; Soldan, Korea), respectively. The four band spectral sensors measured the four spectral bands of blue (400–430 nm), green (540–580 nm), red (630–680 nm), and NIR (800–900 nm) (Kim et al., 2019). Two four-band spectral sensors were installed close to the 4S-SIF (Please see Fig. S6). One sensor was used to measure the incoming signal and the other was used to measure the outgoing signal. We used the ratio of the values obtained by the two sensors to calculate the reflectance. We collected PAR and NDVI at 30-min intervals.

2.6.4. DCMU treatment

We diluted the DCMU to 10^{-4} M in 1% ethanol with water on DOY 290 in the early evening. DCMU selectively binds to photosystem II and block its reoxidation by the plastoquinone pool (Van Rensen, 1989). A DCMU treatment therefore triggers a breakdown in linear photosynthetic electron transport (Ruban et al., 1992), and the resulting excess energy causes an increase in chlorophyll fluorescence emissions (Maxwell and Johnson, 2000). Binding DCMU to photosystem II does not change the leaf pigment composition or canopy structure in the short-term, so we assumed that the spectral reflectance was not affected by the herbicide treatment during the experiment (Rossini et al., 2015). To confirm the effect of DCMU on chlorophyll fluorescence, we measured steady state fluorescence (F_s) using a portable porometer with a pulse-amplitude modulation fluorometer (LI-600; LI-COR). We measured F_s on DOY 289 and 294. For each observation, 25 leaves were randomly selected and observed. To avoid diurnal variation of F_s, we conducted the measurements at 14:00 under clear sky conditions.

3. In-situ SIF observation results

The time series of observed SIF from the reference spectroradiometer and 4S-SIF were similar (Fig. 8). Except for some outliers in the 4S-SIF-based SIF (e.g., DOY 294; Fig. S8), most observed points agreed with the reference spectroradiometer-based SIF in terms of magnitude and pattern over time. The magnitude of the observed SIF from the reference spectroradiometer and 4S-SIF increased after DCMU treatment (DOY 290). Before the DCMU treatment, the maximum observed SIF was 3.57 mW m^{-2} nm^{-1}, while after treatment it was 5.13 mW m^{-2} nm^{-1}. The diurnal variation of the observed SIF from the reference spectroradiometer and 4S-SIF was similar to that of the incoming PAR. However, the magnitude of the incoming PAR was relatively consistent (daily maximum of ~1780 μmol m^{-2} s^{-1}) during the experiment. Therefore, PAR could not explain the increases in SIF observed after the DCMU treatment.

The SIF yield estimated by the reference spectroradiometer and 4S-SIF were strongly correlated (Fig. 9). The R^2 value for the relationship between the daily mean estimated SIF yields from the reference spectroradiometer and 4S-SIF was 0.67, and the relative bias was 5%. The SIF yields estimated by the reference spectroradiometer and 4S-SIF increased significantly after the DCMU treatment. Before the DCMU treatment, the maximum daily mean estimated SIF yield from reference spectroradiometer was around 0.0096 (mW m^{-2} nm^{-1}) / (μmol photons m^{-2} s^{-1}), but it rapidly increased to 0.0126 (mW m^{-2} nm^{-1}) / (μmol photons m^{-2} s^{-1}) after DCMU treatment. In addition, F_s determined from the porometer, i.e., the leaf-level active PAM measurement, also increased after DCMU treatment (Fig. 9). We found that estimated SIF yield value dropped on DOY 290. We used leaf-clip of the active PAM sensor at DOY 289 and the plants might be structurally damaged during the observation. The NDVI time series was consistent regardless of DCMU treatment (Fig. 9). The overall magnitude of the NDVI was around 0.8 over the experimental period.

The SIF yield estimated by the reference spectroradiometer and 4S-SIF increased by a similar percentage after DCMU treatment. The slope of the relationship between the observed SIF and NIR_vP could be used to estimate the SIF yield (Eq. 3) assuming a non-zero intercept (Dechant et al., 2022). When we compared the slope changes based on in-situ observed data under clear sky conditions (DOY 290 and 295), the slope increased by 156% and 148% after DCMU treatment for the reference spectroradiometer and 4S-SIF, respectively (Fig. 10). In addition, the percentage increase was similar to that of the F_s measured by LI-600 (177%; Fig. 9).

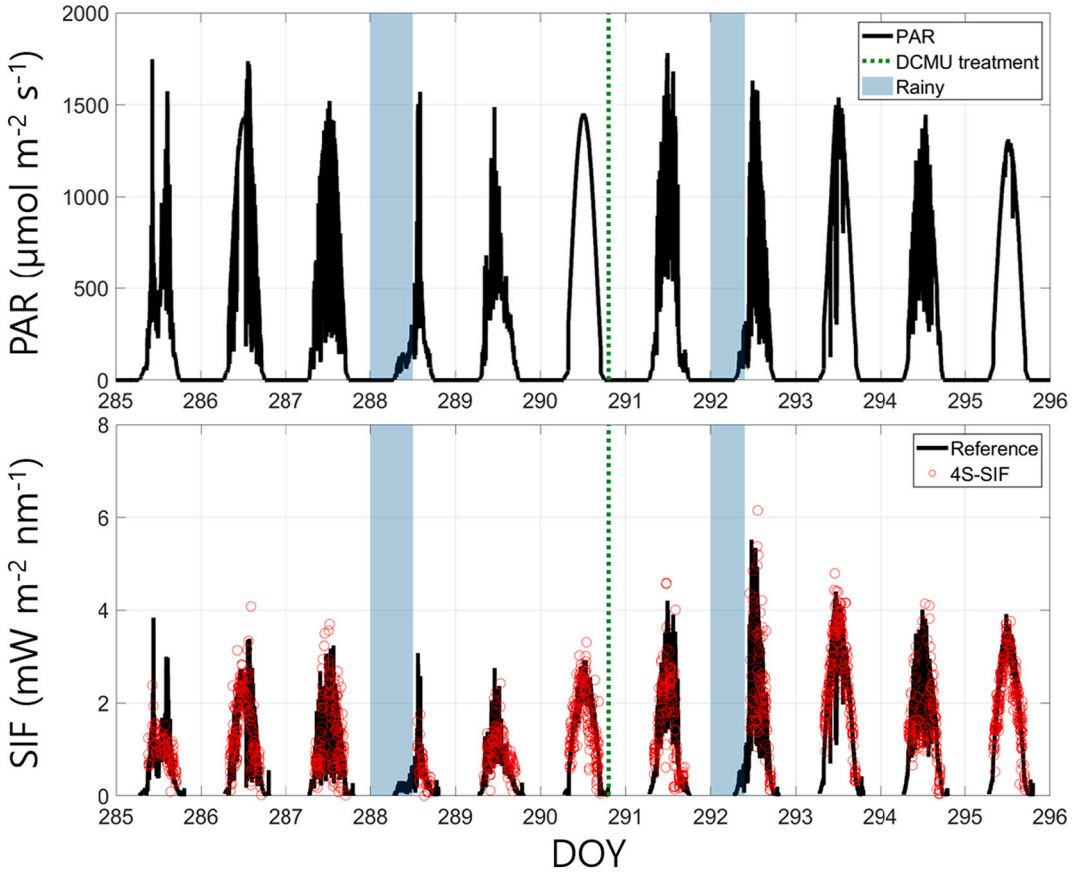

Fig. 8. Temporal dynamics of the incoming PAR and observed SIF from the reference spectroradiometer and 4S-SIF at 1-min intervals. The green dashed line indicates the timing of the DCMU treatment and the blue boxes indicate rainy periods. (For interpretation of the references to colour in this figure legend, the reader is referred to the web version of this article.)

There was a strong linear relationship between the SIF observed by the reference spectroradiometer and 4S-SIF (Fig. 11). Regardless of DCMU treatment, the half-hourly SIF observed by the reference spectroradiometer and 4S-SIF was strongly correlated ($R^2 = 0.85$, rRMSE = 0.22). The correlation between the half-hourly SIF observed by the reference spectroradiometer and 4S-SIF were similar before ($R^2 = 0.73$, rRMSE = 0.27) and after DCMU treatment ($R^2 = 0.85$, rRMSE = 0.2).

4. Discussion

To overcome some of the limitations of the systems currently available for SIF retrieval, we developed the 4S-SIF and installed it in the field to monitor SIF. We then confirmed the reliability of the SIF obtained from 4S-SIF by comparing it to the SIF from the reference spectroradiometer. Here, we comprehensively discuss what we learned while developing the 4S-SIF and address some of the remaining limitations.

4.1. Comparison to previous studies

We devised a filter-based SIF observation system that can be used continuously in the outdoor environment. Previous studies have attempted to estimate SIF by developing systems based on bandpass filters. For example, SIF was previously observed by combining a bandpass filter with an imager sensor and installing it on an airborne platform (Zarco-Tejada et al., 2009), or using two photodiodes, filters, and a beam splitter in a ground-based system (Moya et al., 2004). However, previous studies did not report continuous observed SIF data in the field and also did not check the performance of components under various environmental conditions. In addition, they did not verify the reliability of the observed SIF using dedicated experiments (e.g., the DCMU treatment), which could directly confirm the detection of SIF. In this study, we installed the 4S-SIF in the outdoor environment, collected data continuously, applied a DCMU treatment to induce drastic changes in the chlorophyll fluorescence emission yield, and compared the performance of the newly developed system to a reference spectroradiometer. In addition, we tested the temperature response of the ultra-narrow bandpass filters and found that their transmittance was severely affected by temperature, as reported by the manufacturer (Fig. 6). Our results implied that the temperature response of filter transmittance should be quantified for accurate SIF retrieval because the extracted SIF value could vary with temperature (e.g., as in the 770 nm filter). This was not addressed in previous studies (Moya et al., 2004; Zarco-Tejada et al., 2009). During the outdoor experiment, we were able to correct for the effects of temperature-induced transmittance changes on SIF retrievals (Fig. 7).

4.2. Insights from the sensor development process

Compared to reflectance measurements, high-quality SIF data are much harder to retrieve, which presents a challenge for low-cost sensor development. We have learned the following lessons through the numerous trials and errors involved in the development of the 4S-SIF.

- A photodiode with a flat head was more suitable for SIF retrieval and outdoor use than an LED and photodiode with a round head. Since SIF is a very small signal compared to the incoming PAR and it was difficult to precisely control the angle of incident light in outdoors, it was challenging to use a LED and round-head type photodiode. LED was not sufficiently sensitive and the round-head type photodiode

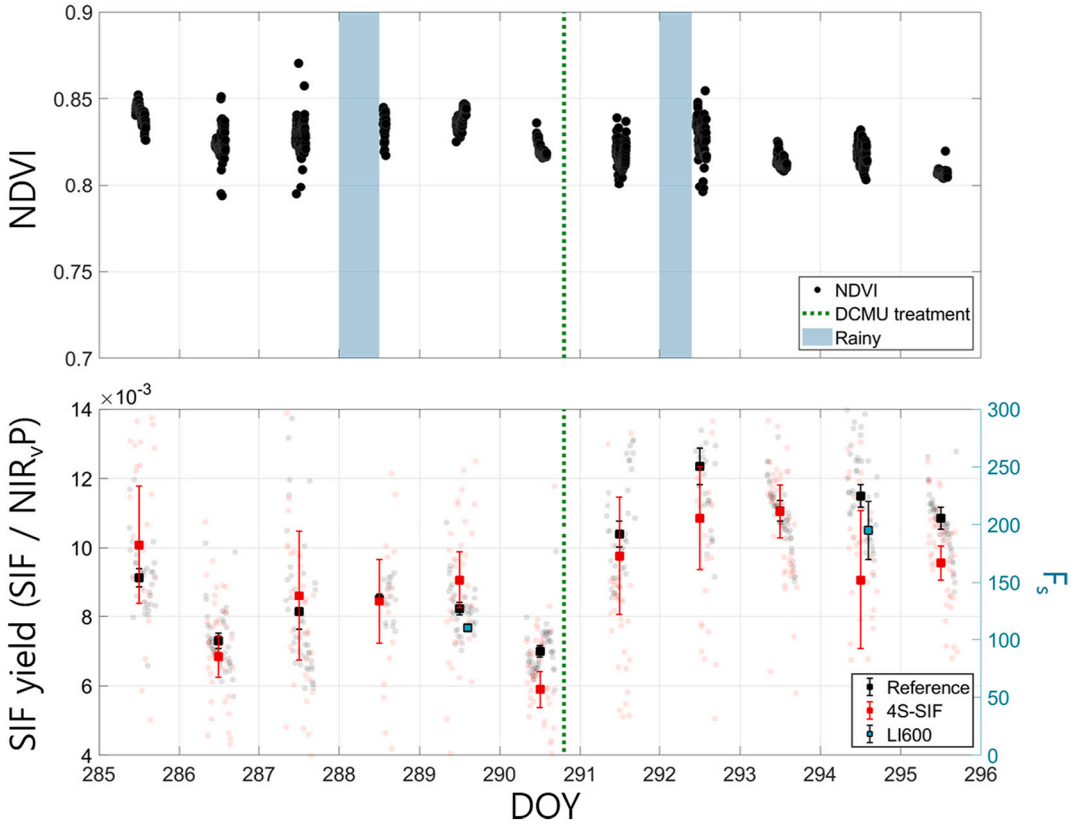

Fig. 9. Time series of NDVI values observed using LED and SIF yield estimated from the steady-state chlorophyll fluorescence (F_s) of the reference spectroradiometer, 4S-SIF, and LI-600 porometer. The green dashed line indicates the timing of DCMU treatment and the blue box plot indicates the rainy period. (For interpretation of the references to colour in this figure legend, the reader is referred to the web version of this article.)

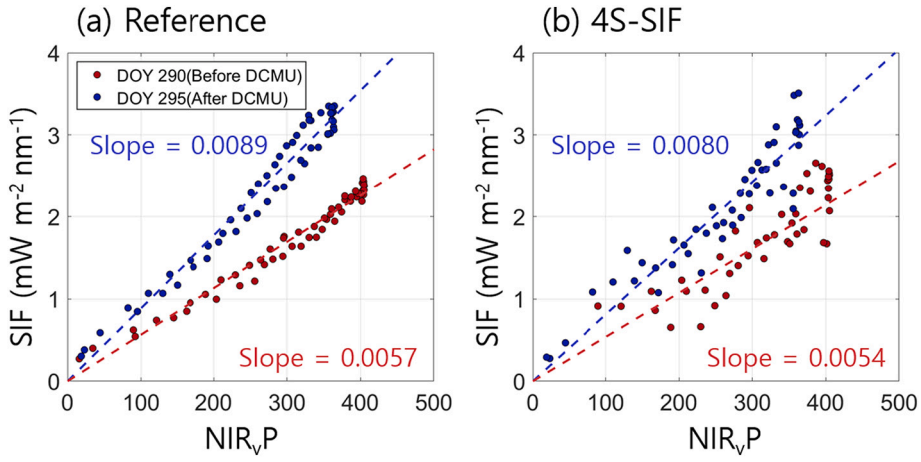

Fig. 10. Relationship between NIR_vP and observed SIF at 10-min intervals under clear sky conditions for the reference spectroradiometer (a) and 4S-SIF (b). The red dots are the observed points and the red line is the result of linear regression before DCMU treatment. The blue dots and dashed line were obtained after DCMU treatment. (For interpretation of the references to colour in this figure legend, the reader is referred to the web version of this article.)

was more sensitive to light with different angles of incidence than a flat-head type (Garrity et al., 2010).

- The use of a collimating lens was essential to increase the amount of light absorbed by the photodiode and reduce the wavelength shift of light passing through the bandpass filter (Please see Fig. S2). Depending on the angle of the incident light, the transmission spectrum passing through the bandpass filter could be "blue-shifted", wherein spectral response features shift to a shorter wavelength (Frey et al., 2015). When the transmittance wavelength shift occurred, the extracted SIF could vary according to the angle of incident light.
- The band-pass filter for specific wavebands does not necessarily ensure that no light will be detected in the other wavelengths (Fig. S9). The one ultra-narrow bandpass filter (optical density = 4) could not sufficiently block light outside of the 710–780 nm range because the light intensity in the O_2A band was much lower than in the other bands. To minimize the amount of transmitted light outside the desired wavelength band, we added a second bandpass filter (section 2.1).

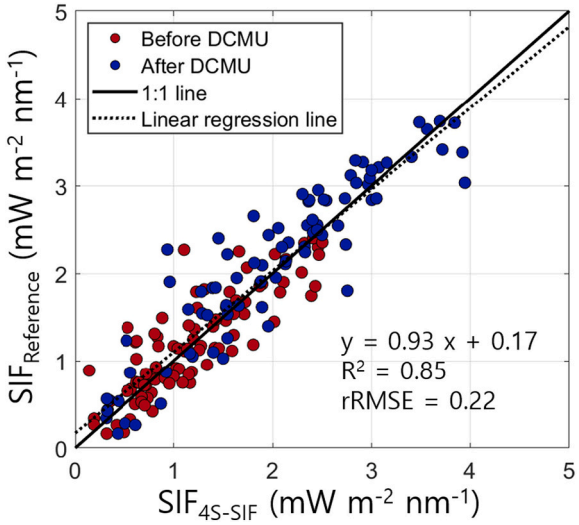

Fig. 11. Relationship between the half-hourly SIF observed by the reference spectroradiometer (using the $3FLD_{one\ pixel}$ method) and 4S-SIF (using the $3FLD_{trans\ applied}$ method) during DOY 285–295. The red dots are the SIF observations before DCMU treatment and the blue dots are the SIF observations after DCMU treatment. (For interpretation of the references to colour in this figure legend, the reader is referred to the web version of this article.)

- The cosine response in diffuse materials must be tested at different light source zenith angles (Fig. 4). For some diffuser materials (e.g., grit ground the glass diffuser), the cosine response for each wavelength could be significantly different (Wu et al., 2019). A small difference in the performance of cosine correctors for each wavelength could be another source of error in SIF retrieval (Marrs et al., 2021). In our system, we used only one diffuser to measure up- and down-welling irradiance with three bands, and the difference was <0.7%; thus, the difference in cosine response among bands might be minor.
- The performance of the ultra-narrow bandpass filter could be affected by temperature, and the degree of change in performance of each ultra-narrow bandpass filter material could be different (Yang et al., 2015). The temperature responses of the filters obtained from two different companies were clearly different (Fig. 6), and it was thus essential to apply the temperature correction (Fig. 7). If the performance of the bandpass filter corresponding to O_2A band was influenced by temperatures like 770 nm, it could affect SIF retrieval significantly.
- It was better to directly measure the dark current than use an empirical equation based on the temperature response thereof. Dark current is one of the most important factors in SIF retrieval (Marrs et al., 2021), and the dark current in photodiodes and optical sensors is affected by temperature (Martyniuk and Rogalski, 2014). Although we could make an empirical relationship between dark current and temperature (Fig. S10), the directly observed dark current would be better for SIF retrieval because the dark current did not change immediately with temperature.
- The photodiode was sensitive not only to light, but also to magnetic fields (Wauters et al., 2009). As we were not aware of this, we invested considerable efforts over a long period of time in developing a customized printed circuit board (PCB) to convert the current generated by photodiode to a DN. However, we could not the achieve adequate performance and therefore we ultimately used a commercial photosensor amplifier; only later did we learn that the signal from the photodiode could be affected by magnetic fields when the ground voltage was not precisely controlled by the customized PCB. Therefore, it was necessary to check whether any noise was caused by the magnetic field that could affect SIF retrieval when using the customized PCB.
- In principle, two 4S-SIF sensors could be used in combination to observe the incoming sunlight and reflected vegetation signals simultaneously, without the need to rotate the single sensor. However, we found that biases were introduced by slight differences in filter transmittances and photodiode sensitivity among sensors, and it was therefore necessary to use a single sensor sequentially for upward and downward measurements.

4.3. The potential of 4S-SIF: trade-offs with spectroradiometers

The 4S-SIF sensor has the potential to overcome high entry barriers in SIF observation. Although using a hyperspectral spectroradiometer enabled us to compare SIF extracted from O_2A, O_2B, and various retrieval methods (Chang et al., 2020; Chang et al., 2021), there are considerable challenges of sensor maintenance in the field as, in addition to radiometric and spectral calibrations, dedicated controls of temperature and humidity are needed. Controlling these variables can be difficult and adds to the cost and complexity of the SIF measurement system. 4S-SIF can help researchers observe SIF in the field more easily. The combination of a photodiode and bandpass filter is relatively easy to use because vegetation indices or SIF can be calculated from the observed signal with a simple equation. For example, there are commercially available sensors that combine a photodiode and bandpass filter (e.g., spectral reflectance sensors; Decagon Devices Inc., USA or Red & Far-Red sensor; Apogee instruments, USA) for measuring the NDVI and PRI (Garrity et al., 2010). This sensor is widely employed because it is easy to use without any knowledge of spectroscopy and has a relatively low purchase price. 4S-SIF also has a similar fundamental structure (combining photodiodes and bandpass filters) to commercial spectral reflectance sensors (Fig. 1). Furthermore, 4S-SIF has the potential to be used to observe light in a desired wavelength bands by selectively changing the filters. We anticipate that the information deposited in our GitHub repository will help the research community replicate or improve the system.

Recently, the importance of the differences in the SIF observation methods (e.g, the hemispherical-conical and bi-hemispherical systems) was highlighted (Chang et al., 2021). 4S-SIF can potentially be used to explore the differences in SIF observation methods. The current 4S-SIF is a bi-hemispherical system, but if an additional structure is combined with the diffuser to constrain the view angle as in a previous study (Garrity et al., 2010), it has the potential to be used as a hemispherical-conical system.

4.4. Limitations of 4S-SIF

Despite the overall success of SIF retrieval from the 4S-SIF sensor, there were several limitations.

First, in the simulation for SIF retrievals under a changing temperature, we found that the slope of the relationship between the temperature and extracted SIF changed slightly according to the magnitude of the simulated input SIF value (Fig. S11). To quantify the effect of the magnitude of the simulated input SIF following a temperature correction, we conducted further analyses based on observed the spectral data in various temperatures (Figs. S11–S13 in the supplementary materials). Although there was no clear difference between temperature-corrected SIF and non-corrected SIF at the diurnal time scale (Fig. S12) and might not have a significant effect on the extracted SIF (Fig. S13), a comparison of additional long-term 4S-SIF observations with SIF obtained from a reference spectrometer system is necessary for more reliable verification of 4S-SIF.

Second, rotating the whole 4S-SIF sensor to switch between the upward and downward observations tended to introduce a longer time lag when matching the observations in the two directions than other approaches, such as the use of two spectrometers or an optical switching

approach, as in the Fluospec and rotating-prism systems (Kim et al., 2021; Yang et al., 2018c). Although the overall system cost could be reduced by observing up- and down-welling irradiance simultaneously using a single sensor, the uncertainty of the extracted SIF on cloudy days when incoming irradiance rapidly changes can increase due to the longer time lag.

Third, 4S-SIF can only use FLD-type retrieval methods, which have limitations as FLD-based SIF cannot capture SIF variations well during cloudy periods. According to Chang et al. (2020), 3FLD-based SIF showed relatively poor performance compared to spectral fitting method, singular vector decomposition and differential optical absorption spectroscopy retrieval method. Atmospheric correction may also be required depending on the distance between the sensor and top of the canopy (Cendrero-Mateo et al., 2019; Sabater et al., 2018; Vicent et al., 2017), and FLD-based SIF could be affected by the spectral shape of the reflected irradiance (Meroni et al., 2009). We found that the filter-based SIF retrieval method was strongly affected by the spectral shape of the reflected irradiance (Fig. 3). We also found that $3FLD_{trans\ applied}$-based SIF had a lower R^2 value and higher rRMSE than $3FLD_{one\ pixel}$-based SIF (Fig. 3). This was because the $3FLD_{trans\ applied}$-based SIF varied considerably depending on the magnitude of the incoming irradiance and steepness of the spectral shape under the same SIF value (Fig. S14). Furthermore, the $3FLD_{trans\ applied}$-based SIF could show a negative value when the chlorophyll fluorescence yield value was low in the winter (Fig. S15) and the relationship between the $3FLD_{trans\ applied}$- and $3FLD_{one\ pixel}$-based SIF could be changed (Fig. S15). This limitation could potentially be resolved to some extent by using a different ultra-narrow bandpass filter. In fact, we investigated the effect of changing the FWHM and center wavelength of the filters corresponding to "out" in 3FLD on $3FLD_{trans\ applied}$-based SIF retrieval through a simulation (Appendix D). We observed an increase in the R^2 value (from 0.87 to 0.94) and decrease in rRMSE (from 41% to 27%) when we changed the filter transmittance from the 770 nm filter to the 780 nm center wavelength with the same transmittance as the 757 nm filter (Fig. S16). Therefore, the effect of spectral shape on filter-based SIF retrieval could be reduced by optimizing the filter characteristics, such as the FWHM and center wavelength. Alternatively, a correction method based on simulations or empirical equations based on long-term observations could be developed (Nakashima et al., 2021).

Fourth, the SIF retrieved from 4S-SIF contained more noise than the SIF from the reference spectroradiometer (Figs. 3, 9, and 10). This could be a limitation when investigating subtle changes in diurnal patterns or analyzing patterns of Φ_F. In fact, we found that the signal to noise ratio (SNR) from 4S-SIF was not as high as that of the reference spectroradiometer (Fig. S17). Although the effect of noise was drastically reduced when we averaged >40 samples (Fig. S18), there are still limitations in our method of estimating the SNR of 4S-SIF as the environmental conditions were not controlled well. Therefore, it is necessary to quantify the SNR of 4S-SIF changes under various environmental conditions and in the laboratory, and to better quantify the effect of SNR on SIF retrieval through simulations and observation in a similar way as done in Damm et al. (2011). Further refinements of 4S-SIF could improve the SNR, and thus lead to higher-quality SIF retrievals.

5. Conclusion

Ground-based SIF observations in multiple locations and biomes are necessary to better understand and explain the mechanisms underlying the remote sensing of SIF. We developed the 4S-SIF sensor to continuously monitor canopy-level SIF. 4S-SIF combines ultra-narrow bandpass filters and uses a photodiode as a detector. We confirmed that the 4S-SIF displayed a linear response to light intensity compared to the reference spectroradiometer and had a close-to-optimal cosine response curve to incoming light for all the spectral bands involved in the SIF retrieval. In addition, we measured the temperature response of ultra-narrow bandpass filters and corrected it based on simulations. We installed the 4S-SIF and reference spectroradiometer in a strawberry plot to confirm that developed system could detect the SIF signal. The SIF retrieved from the 4S-SIF agreed well with that obtained from the reference sensor before and after a herbicide treatment. We believe that 4S-SIF will be a useful tool for collecting in-situ data across multiple spatial and temporal scales and anticipate that our experience in developing 4S-SIF will be useful for researchers designing similar sensors.

Author contribution

Jongmin Kim = Idea, Paper concept, Sensor development, Data acquisition, Data analyses, Writing, Interpretation of the result.

Youngryel Ryu = Idea, Paper concept, Funding acquisition, Project administration, Writing, Interpretation of the result.

Benjamin Dechant = Idea, Paper concept, Sensor development, Data analyses, Writing, Interpretation of the result.

Declaration of Competing Interest

None.

Data availability

All scripts are open to public via github

Acknowledgments

This study was supported by the National Research Foundation of Korea (NRF-2017K1A3A1A12072870), Korea Environment Industry & Technology Institute (KEITI) through its Urban Ecological Health Promotion Technology Development Project, funded by the Korea Ministry of Environment (MOE) (2019002760002) and Rural Development Administration, Republic of Korea (PJ017023). B. Dechant acknowledges support from sDiv, the Synthesis Centre of iDiv (DFG FZT 118, 202548816). We thank Oliver Sonnentag and Elyn Humphreys for their support. We are also grateful for the constructive comments of Joseph Berry and Pablo J. Zarco-Tejada, and the contribution of Yorum Hwang to the production of Fig. 1. We have uploaded the details of 4S-SIF to our GitHub repository (https://kimhyodong.com/github/).

Appendix A. List of components (prices as of 2020–2021 in South Korea)

Table A1
List of components.

Component	Item	Company	Q'ty	Unit price (USD)
Photodiode	S2386-18 K	Hamamatsu Photonics	1	$1.88
Photosensor amplifier	C9329	Hamamatsu Photonics	1	$1298
Diffuser	White diffusing glass	Edmund Optics	1	$43.5
Collimating lens	LA1540-ML	Thorlabs	1	$38.55
Ultra-narrow bandpass filter for 757 nm	757.9–1 OD4	Alluxa	1	$1160.7

(*continued on next page*)

Table A1 (*continued*)

Component	Item	Company	Q'ty	Unit price (USD)
Ultra-narrow bandpass filter for 761 nm	760.7–1 OD4	Alluxa	1	$910
Bandpass filter for 761 nm	745BP70	Omega Optical	1	$409.67
Ultra-narrow bandpass filter for 770 nm	770NB	Omega Optical	1	$329
Geared motor	GGM DC 12 V 3000 rpm	GGM	1	$49.16
Servomotor	PDI-6225MG-300	JX	1	$2.46
Microcomputer	Raspberry Pi b3 module	Raspberry Pi foundation	1	$41
Temperature and humidity sensor	DHT22	Adafruit	1	$0.33
Fan	DC brushless	Jameco electronics	2	$21.6
Micro SD card 16 GB	SD card	Samsung	1	$17.2
The 3D structure	PET material	–	1	$20.5
Sum				**$4343.55**

Appendix B. Relationship between the SIF values retrieved from the one-pixel-based 3FLD method ($3FLD_{one\ pixel}$) and filter transmittance-based 3FLD method ($3FLD_{trans\ applied}$)

The SIF value extracted using $3FLD_{trans\ applied}$ was much lower than that obtained from $3FLD_{one\ pixel}$ (the slope of the relationship was 25.07; Fig. B1). The irradiance in $3FLD_{trans\ applied}$ had a wider wavelength range than that in $3FLD_{one\ pixel}$; thus, the magnitude of the extracted SIF value could differ. To correct the magnitude of the SIF value from the 4S-SIF, we used the relationship between the SIF using only one pixel from the spectral data ($3FLD_{one\ pixel}$) and applied transmittance ($3FLD_{trans\ applied}$) to the spectral data observed by the reference spectroradiometer at DOY 293. There was a strong linear relationship between the two methods. Using the derived equation, we corrected the SIF from the 4S-SIF.

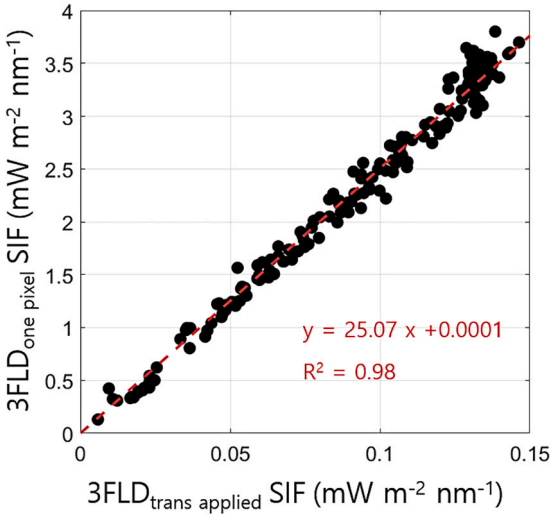

Fig. B1. Relationship between SIF from $3FLD_{trans\ applied}$ and $3FLD_{one\ pixel}$.

Appendix C. Images used in the outdoor experiment

Images of a strawberry canopy were obtained using a micro-camera module (Camera module V2; Raspberry Pi) (Kim et al., 2019), every day at noon. We confirmed that there were no significant structural changes in the strawberry images after DCMU treatment (DOY 290).

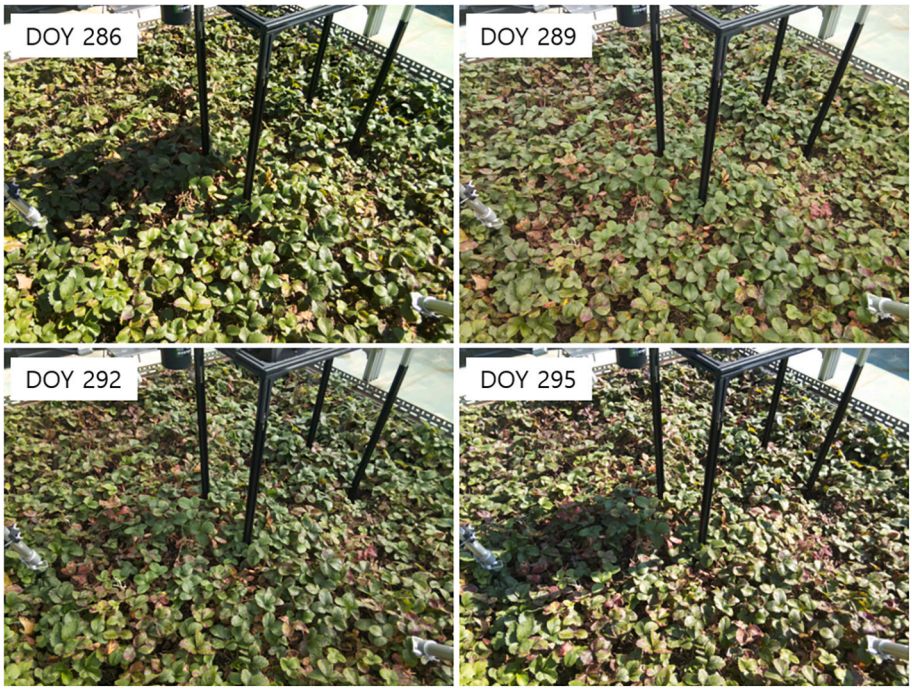

Fig. C1. Images from the outdoor experiment.

Appendix D. Simulation results obtained using different ultra-narrow bandpass filters

We investigated the effect of the FWHM and center wavelength of the two "out" irradiations on the SIF retrieval based on the $3FLD_{trans\ applied}$ method. We used the same simulation method described in section 2.2. We only changed the center wavelengths and FWHM of the transmittance corresponding to the left and right "out" in the 3FLD method. To simulate the transmittance for the left and right "out", we used the transmittance from the 757 nm filter. We fitted the transmittance from the 757 nm filter using a one-term Gaussian model. We changed the FWHM of the fitted transmittance using the *nthroot function* in Matlab. We used the fixed transmittance from the 761 nm filter for "in" for the O_2A band. The R^2 value and rRMSE clearly changed according to the FWHM and center wavelength of transmittance (Fig. D1 and Fig. S16).

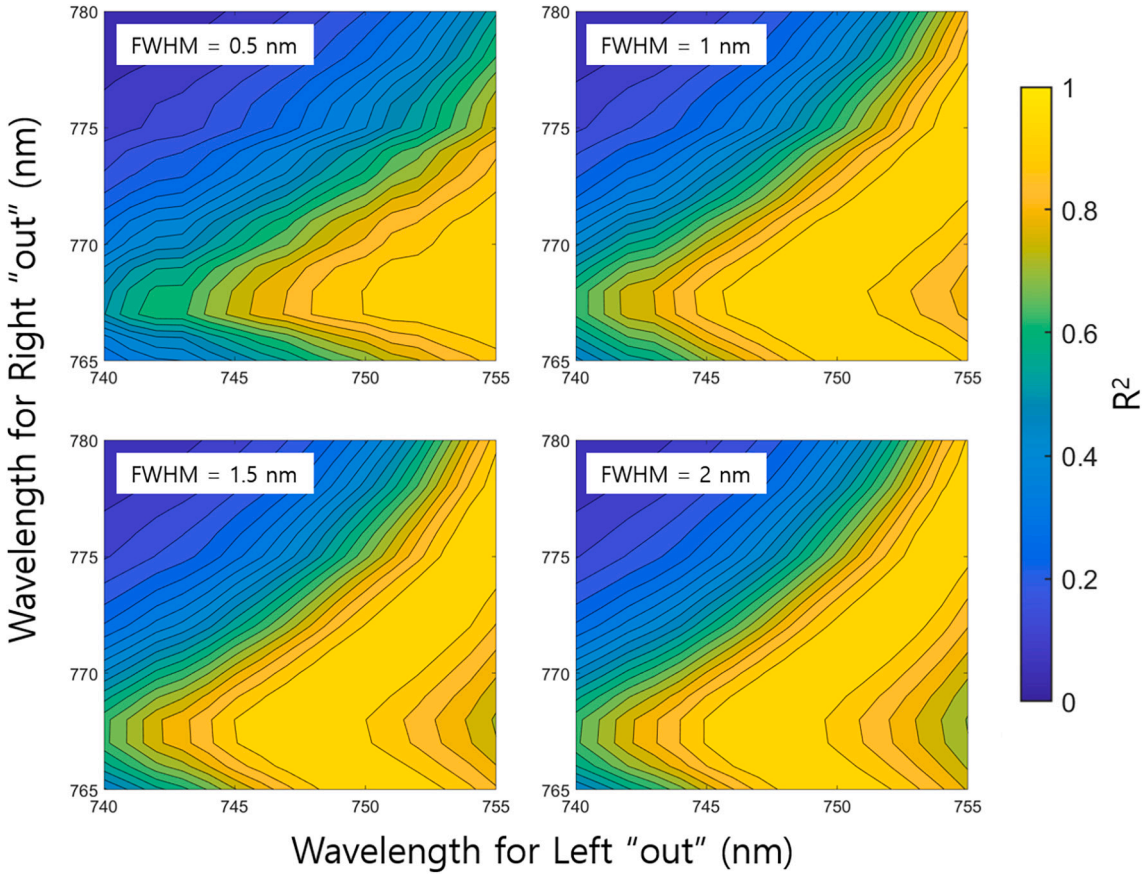

Fig. D1. Contour maps of the coefficient of determination (R^2) between the simulated and extracted SIF, using the 3FLD method and different wavelengths and FWHM on the left and right "'out".

Appendix E. Supplementary data

Supplementary data to this article can be found online at https://doi.org/10.1016/j.rse.2022.113311.

References

Alemohammad, S.H., et al., 2017. Water, Energy, and Carbon with Artificial Neural Networks (WECANN): a statistically-based estimate of global surface turbulent fluxes and gross primary productivity using solar-induced fluorescence. Biogeosciences 14 (18), 4101 (Online).

Badgley, G., Field, C.B., Berry, J.A., 2017. Canopy near-infrared reflectance and terrestrial photosynthesis. Sci. Adv. 3 (3), e1602244.

Baldocchi, D.D., et al., 2020. Outgoing near-infrared radiation from vegetation scales with canopy photosynthesis across a spectrum of function, structure, physiological capacity, and weather. <sb:contribution><sb:title>J. Geophys. Res. </sb:title></sb:contribution><sb:host><sb:issue><sb:series><sb:title>Biogeosci.</sb:title></sb:series></sb:issue></sb:host> 125 (7), e2019JG005534.

Belwalkar, A., et al., 2022. Evaluation of SIF retrievals from narrow-band and sub-nanometer airborne hyperspectral imagers flown in tandem: modelling and validation in the context of plant phenotyping. Remote Sens. Environ. 273, 112986.

Burkart, A., et al., 2015. A method for uncertainty assessment of passive sun-induced chlorophyll fluorescence retrieval using an infrared reference light. IEEE Sensors J. 15 (8), 4603–4611.

Campbell, P.K.E., et al., 2019. Diurnal and seasonal variations in chlorophyll fluorescence associated with photosynthesis at leaf and canopy scales. Remote Sens. 11 (5), 488.

Cendrero-Mateo, M.P., et al., 2019. Sun-induced chlorophyll fluorescence III: benchmarking retrieval methods and sensor characteristics for proximal sensing. Remote Sens. 11 (8), 962.

Chang, C.Y., Guanter, L., Frankenberg, C., Köhler, P., Gu, L., Magney, T.S., Sun, Y., 2020. Systematic assessment of retrieval methods for canopy far-red solar-induced chlorophyll fluorescence (SIF) using high-frequency automated field spectroscopy. J. Geophys.Res.Biogeosci. 125 (7), e2019JG005533.

Chang, C.Y., et al., 2021. Unpacking the drivers of diurnal dynamics of sun-induced chlorophyll fluorescence (SIF): canopy structure, plant physiology, instrument configuration and retrieval methods. Remote Sens. Environ. 265, 112672.

Cheng, Y.-B., et al., 2013. Integrating solar induced fluorescence and the photochemical reflectance index for estimating gross primary production in a cornfield. Remote Sens. 5 (12), 6857–6879.

Cogliati, S., et al., 2015. Continuous and long-term measurements of reflectance and sun-induced chlorophyll fluorescence by using novel automated field spectroscopy systems. Remote Sens. Environ. 164, 270–281.

Damm, A., et al., 2010. Remote sensing of sun-induced fluorescence to improve modeling of diurnal courses of gross primary production (GPP). Glob. Chang. Biol. 16 (1), 171–186.

Damm, A., et al., 2011. Modeling the impact of spectral sensor configurations on the FLD retrieval accuracy of sun-induced chlorophyll fluorescence. Remote Sens. Environ. 115 (8), 1882–1892.

Daumard, F., et al., 2010. A field platform for continuous measurement of canopy fluorescence. IEEE Trans. Geosci. Remote Sens. 48 (9), 3358–3368.

Dechant, B., et al., 2022. NIRVP: a robust structural proxy for sun-induced chlorophyll fluorescence and photosynthesis across scales. Remote Sens. Environ. 268, 112763.

Dechant, B., et al., 2020. Canopy structure explains the relationship between photosynthesis and sun-induced chlorophyll fluorescence in crops. Remote Sens. Environ. 241, 111733.

Du, S., et al., 2019. SIFSpec: measuring solar-induced chlorophyll fluorescence observations for remote sensing of photosynthesis. Sensors 19 (13), 3009.

Frankenberg, C., Berry, J., 2018. Solar induced chlorophyll fluorescence: origins, relation to photosynthesis and retrieval.

Frankenberg, C., et al., 2011. New global observations of the terrestrial carbon cycle from GOSAT: patterns of plant fluorescence with gross primary productivity. Geophys. Res. Lett. 38 (17).

Frey, L., Masarotto, L., Armand, M., Charles, M.-L., Lartigue, O., 2015. Multispectral interference filter arrays with compensation of angular dependence or extended spectral range. Opt. Express 23 (9), 11799–11812.

Gamon, J., Kovalchuck, O., Wong, C., Harris, A., Garrity, S., 2015. Monitoring seasonal and diurnal changes in photosynthetic pigments with automated PRI and NDVI sensors. Biogeosciences 12 (13), 4149–4159.

Gamon, J., Serrano, L., Surfus, J., 1997. The photochemical reflectance index: an optical indicator of photosynthetic radiation use efficiency across species, functional types, and nutrient levels. Oecologia 112 (4), 492–501.
Garrity, S.R., Vierling, L.A., Bickford, K., 2010. A simple filtered photodiode instrument for continuous measurement of narrowband NDVI and PRI over vegetated canopies. Agric. For. Meteorol. 150 (3), 489–496.
Goulas, Y., et al., 2017. Gross primary production of a wheat canopy relates stronger to far red than to red solar-induced chlorophyll fluorescence. Remote Sens. 9 (1), 97.
Grossmann, K., et al., 2018. PhotoSpec: a new instrument to measure spatially distributed red and far-red solar-induced chlorophyll fluorescence. Remote Sens. Environ. 216, 311–327.
Gu, L., Wood, J.D., Chang, C.Y., Sun, Y., Riggs, J.S., 2019. Advancing terrestrial ecosystem science with a novel automated measurement system for sun-induced chlorophyll fluorescence for integration with eddy covariance flux networks. Journal of Geophysical Research: Biogeosciences 124 (1), 127–146.
Hampel, F.R., 1974. The influence curve and its role in robust estimation. J. Am. Stat. Assoc. 69 (346), 383–393.
Hueni, A., Bialek, A., 2017. Cause, effect, and correction of field spectroradiometer interchannel radiometric steps. IEEE J.Sel.Top.Appl.Earth Obs.Remote Sens. 10 (4), 1542–1551.
Jacquemoud, S., Baret, F., 1990. PROSPECT: a model of leaf optical properties spectra. Remote Sens. Environ. 34 (2), 75–91.
Jacquemoud, S., et al., 2009. PROSPECT+ SAIL models: a review of use for vegetation characterization. Remote Sens. Environ. 113, S56–S66.
Jeong, S.-J., et al., 2017. Application of satellite solar-induced chlorophyll fluorescence to understanding large-scale variations in vegetation phenology and function over northern high latitude forests. Remote Sens. Environ. 190, 178–187.
Joiner, J., et al., 2013. Global monitoring of terrestrial chlorophyll fluorescence from moderate-spectral-resolution near-infrared satellite measurements: methodology, simulations, and application to GOME-2. Atmos.Meas.Tech. 6 (10), 2803–2823.
Joiner, J., et al., 2014. The seasonal cycle of satellite chlorophyll fluorescence observations and its relationship to vegetation phenology and ecosystem atmosphere carbon exchange. Remote Sens. Environ. 152, 375–391.
Julitta, T., et al., 2016. Comparison of sun-induced chlorophyll fluorescence estimates obtained from four portable field spectroradiometers. Remote Sens. 8 (2), 122.
Kebabian, P.L., Theisen, A.F., Kallelis, S., Freedman, A., 1999. A passive two-band sensor of sunlight-excited plant fluorescence. Rev. Sci. Instrum. 70 (11), 4386–4393.
Kim, J., et al., 2021. Solar-induced chlorophyll fluorescence is non-linearly related to canopy photosynthesis in a temperate evergreen needleleaf forest during the fall transition. Remote Sens. Environ. 258, 112362.
Kim, J., Ryu, Y., Jiang, C., Hwang, Y., 2019. Continuous observation of vegetation canopy dynamics using an integrated low-cost, near-surface remote sensing system. Agric. For. Meteorol. 264, 164–177.
Lee, S., Ryu, Y., Jiang, C., 2015. Urban heat mitigation by roof surface materials during the East Asian summer monsoon. Environ. Res. Lett. 10 (12), 124012.
Li, X., Xiao, J., 2022. TROPOMI observations allow for robust exploration of the relationship between solar-induced chlorophyll fluorescence and terrestrial gross primary production. Remote Sens. Environ. 268, 112748.
Liu, X., Liu, L., 2018. Influence of the canopy BRDF characteristics and illumination conditions on the retrieval of solar-induced chlorophyll fluorescence. Int. J. Remote Sens. 39 (6), 1782–1799.
Liu, X., et al., 2021. Modelling the influence of incident radiation on the SIF-based GPP estimation for maize. Agric. For. Meteorol. 307, 108522.
Louis, J., et al., 2005. Remote sensing of sunlight-induced chlorophyll fluorescence and reflectance of Scots pine in the boreal forest during spring recovery. Remote Sens. Environ. 96 (1), 37–48.
Lu, X., et al., 2018. Comparison of phenology estimated from reflectance-based indices and solar-induced chlorophyll fluorescence (SIF) observations in a temperate forest using GPP-based phenology as the standard. Remote Sens. 10 (6), 932.
Magney, T.S., et al., 2019. Mechanistic evidence for tracking the seasonality of photosynthesis with solar-induced fluorescence. Proc. Natl. Acad. Sci. 116 (24), 11640–11645.
Magney, T.S., Eitel, J.U., Huggins, D.R., Vierling, L.A., 2016. Proximal NDVI derived phenology improves in-season predictions of wheat quantity and quality. Agric. For. Meteorol. 217, 46–60.
Marcolla, B., Cescatti, A., 2018. Geometry of the hemispherical radiometric footprint over plant canopies. Theor. Appl. Climatol. 134 (3), 981–990.
Marrs, J.K., Jones, T.S., Allen, D.W., Hutyra, L.R., 2021. Instrumentation sensitivities for tower-based solar-induced fluorescence measurements. Remote Sens. Environ. 259, 112413.
Martini, D., Sakowska, K., Wohlfahrt, G., Pacheco-Labrador, J., van der Tol, C., Porcar-Castell, A., Migliavacca, M., 2022. Heatwave breaks down the linearity between sun-induced fluorescence and gross primary production. New Phytol. 233 (6), 2415–2428.
Martyniuk, P., Rogalski, A., 2014. Performance comparison of barrier detectors and HgCdTe photodiodes. Opt. Eng. 53 (10), 106105.
Maxwell, K., Johnson, G.N., 2000. Chlorophyll fluorescence—a practical guide. J. Exp. Bot. 51 (345), 659–668.
Meroni, M., Colombo, R., 2006. Leaf level detection of solar induced chlorophyll fluorescence by means of a subnanometer resolution spectroradiometer. Remote Sens. Environ. 103 (4), 438–448.
Meroni, M., et al., 2009. Remote sensing of solar-induced chlorophyll fluorescence: review of methods and applications. Remote Sens. Environ. 113 (10), 2037–2051.
Miao, G., et al., 2018. Sun-induced chlorophyll fluorescence, photosynthesis, and light use efficiency of a soybean field from seasonally continuous measurements. J. Geophys.Res.Biogeosci. 123 (2), 610–623.
Migliavacca, M., et al., 2017. Plant functional traits and canopy structure control the relationship between photosynthetic CO 2 uptake and far-red sun-induced fluorescence in a Mediterranean grassland under different nutrient availability. New Phytol. 214 (3), 1078–1091.
Mohammed, G.H., et al., 2019. Remote sensing of solar-induced chlorophyll fluorescence (SIF) in vegetation: 50 years of progress. Remote Sens. Environ. 231, 111177.
Moya, I., et al., 2004. A new instrument for passive remote sensing: 1. Measurements of sunlight-induced chlorophyll fluorescence. Remote Sens. Environ. 91 (2), 186–197.
Nakashima, N., et al., 2021. Area-ratio Fraunhofer line depth (aFLD) method approach to estimate solar-induced chlorophyll fluorescence in low spectral resolution spectra in a cool-temperate deciduous broadleaf forest. J. Plant Res. 134 (4), 713–728.
Nichol, C.J., et al., 2019. Diurnal and seasonal solar induced chlorophyll fluorescence and photosynthesis in a boreal scots pine canopy. Remote Sens. 11 (3), 273.
Pacheco-Labrador, J., et al., 2019. Sun-induced chlorophyll fluorescence I: instrumental considerations for proximal spectroradiometers. Remote Sens. 11 (8), 960.
Pacheco-Labrador, J., Martín, M., 2015. Characterization of a field spectroradiometer for unattended vegetation monitoring. Key sensor models and impacts on reflectance. Sensors 15 (2), 4154–4175.
Paul-Limoges, E., et al., 2018. Effect of environmental conditions on sun-induced fluorescence in a mixed forest and a cropland. Remote Sens. Environ. 219, 310–323.
Pierrat, Z., et al., 2022. Diurnal and seasonal dynamics of solar-induced chlorophyll fluorescence, vegetation indices, and gross primary productivity in the boreal forest. <sb:contribution><sb:title>J. Geophys. Res. </sb:title></sb:contribution><sb:host><sb:issue><sb:series><sb:title>Biogeosci.</sb:title></sb:series></sb:issue></sb:host> 127 (2), e2021JG006588.
Pinto, F., et al., 2020. Dynamics of sun-induced chlorophyll fluorescence and reflectance to detect stress-induced variations in canopy photosynthesis. Plant Cell Environ. 43 (7), 1637–1654.
Plascyk, J.A., 1975. The MK II Fraunhofer Line Discriminator (FLD-II) for Airborne And Orbital Remote Sensing of Solar-stimulated Luminescence, 14. SPIE.
Pontailler, J.-Y., Hymus, G.J., Drake, B.G., 2003. Estimation of leaf area index using ground-based remote sensed NDVI measurements: validation and comparison with two indirect techniques. Can. J. Remote. Sens. 29 (3), 381–387.
Pontailler, J.Y., Genty, B., 1996. A simple red: far-red sensor using gallium arsenide phosphide detectors. Funct. Ecol. 10 (4), 535–540.
Renhorn, I.G., Bergström, D., Hedborg, J., Letalick, D., Möller, S., 2016. High spatial resolution hyperspectral camera based on a linear variable filter. Opt. Eng. 55 (11), 114105.
Richardson, A.D., Braswell, B.H., Hollinger, D.Y., Jenkins, J.P., Ollinger, S.V., 2009. Near-surface remote sensing of spatial and temporal variation in canopy phenology. Ecol. Appl. 19 (6), 1417–1428.
Rienstra, J.L., 1998. Transformation of filter transmission data for f-number and chief ray angle. In: Infrared Imaging Systems: Design, Analysis, Modeling, And Testing IX. International Society for Optics and Photonics, pp. 267–275.
Rossini, M., et al., 2010. High resolution field spectroscopy measurements for estimating gross ecosystem production in a rice field. Agric. For. Meteorol. 150 (9), 1283–1296.
Rossini, M., et al., 2015. Red and far red sun-induced chlorophyll fluorescence as a measure of plant photosynthesis. Geophys. Res. Lett. 42 (6), 1632–1639.
Ruban, A., Rees, D., Pascal, A., Horton, P., 1992. Mechanism of ΔpH-dependent dissipation of absorbed excitation energy by photosynthetic membranes. II. The relationship between LHCII aggregation in vitro and qE in isolated thylakoids. BBA-Bioenergetics 1102 (1), 39–44.
Ryu, Y., et al., 2010. Testing the performance of a novel spectral reflectance sensor, built with light emitting diodes (LEDs), to monitor ecosystem metabolism, structure and function. Agric. For. Meteorol. 150 (12), 1597–1606.
Ryu, Y., Berry, J.A., Baldocchi, D.D., 2019. What is global photosynthesis? History, uncertainties and opportunities. Remote Sens. Environ. 223, 95–114.
Sabater, N., et al., 2018. Compensation of oxygen transmittance effects for proximal sensing retrieval of canopy–leaving sun–induced chlorophyll fluorescence. Remote Sens. 10 (10), 1551.
Soudani, K., et al., 2012. Ground-based network of NDVI measurements for tracking temporal dynamics of canopy structure and vegetation phenology in different biomes. Remote Sens. Environ. 123, 234–245.
Sun, Y., et al., 2018. Overview of Solar-Induced chlorophyll Fluorescence (SIF) from the Orbiting Carbon Observatory-2: retrieval, cross-mission comparison, and global monitoring for GPP. Remote Sens. Environ. 209, 808–823.
Sun, Y., et al., 2017. OCO-2 advances photosynthesis observation from space via solar-induced chlorophyll fluorescence. Science 358 (6360), eaam5747.
Van der Tol, C., Berry, J., Campbell, P., Rascher, U., 2014. Models of fluorescence and photosynthesis for interpreting measurements of solar-induced chlorophyll fluorescence. J.Geophys.Res.Biogeosci. 119 (12), 2312–2327.
Van der Tol, C., Verhoef, W., Timmermans, J., Verhoef, A., Su, Z., 2009. An integrated model of soil-canopy spectral radiances, photosynthesis, fluorescence, temperature and energy balance. Biogeosciences 6 (12), 3109–3129.
Van Rensen, J., 1989. Herbicides interacting with photosystem II. In: Herbicides And Plant Metabolism, pp. 21–36.
Verhoef, W., 1984. Light scattering by leaf layers with application to canopy reflectance modeling: the SAIL model. Remote Sens. Environ. 16 (2), 125–141.
Vicent, J., Sabater, N., Verrelst, J., Alonso, L., Moreno, J., 2017. Assessment of approximations in aerosol optical properties and vertical distribution into FLEX atmospherically-corrected surface reflectance and retrieved sun-induced fluorescence. Remote Sens. 9 (7), 675.
Vilfan, N., Van der Tol, C., Muller, O., Rascher, U., Verhoef, W., 2016. Fluspect-B: a model for leaf fluorescence, reflectance and transmittance spectra. Remote Sens. Environ. 186, 596–615.

Walther, S., et al., 2016. Satellite chlorophyll fluorescence measurements reveal large-scale decoupling of photosynthesis and greenness dynamics in boreal evergreen forests. Glob. Chang. Biol. 22 (9), 2979–2996.
Wang, H., Song, H., Chen, Y., Laney, S.R., 2015. Correcting temperature dependence in miniature spectrometers used in cold polar environments. Appl. Opt. 54 (11), 3162–3172.
Wauters, F., et al., 2009. Performance of silicon PIN photodiodes at low temperatures and in high magnetic fields. Nucl. Instrum. Methods Phys. Res., Sect. A 604 (3), 563–567.
Wieneke, S., et al., 2018a. Linking photosynthesis and sun-induced fluorescence at sub-daily to seasonal scales. Remote Sens. Environ. 219, 247–258.
Wieneke, S., et al., 2018b. Linking photosynthesis and sun-induced fluorescence at sub-daily to seasonal scales. Remote Sens. Environ. 219, 247–258.
Wohlfahrt, G., et al., 2018. Sun-induced fluorescence and gross primary productivity during a heat wave. Sci. Rep. 8 (1), 14169.
Wu, H., Cheng, H., Feng, Y., 2019. Design of a free-form diffuser for the entrance optic to correct the cosine error in the photometer. Appl. Opt. 58 (18), 5029–5039.
Xu, S., et al., 2021. Structural and photosynthetic dynamics mediate the response of SIF to water stress in a potato crop. Remote Sens. Environ. 263, 112555.
Yang, J., et al., 2018a. Amazon drought and forest response: largely reduced forest photosynthesis but slightly increased canopy greenness during the extreme drought of 2015/2016. Glob. Chang. Biol. 24 (5), 1919–1934.
Yang, J.C., et al., 2022. Gross primary production (GPP) and red solar induced fluorescence (SIF) respond differently to light and seasonal environmental conditions in a subalpine conifer forest. Agric. For. Meteorol. 317, 108904.
Yang, K., et al., 2018b. Sun-induced chlorophyll fluorescence is more strongly related to absorbed light than to photosynthesis at half-hourly resolution in a rice paddy. Remote Sens. Environ. 216, 658–673.
Yang, P., van der Tol, C., 2018. Linking canopy scattering of far-red sun-induced chlorophyll fluorescence with reflectance. Remote Sens. Environ. 209, 456–467.
Yang, P., van der Tol, C., Campbell, P.K., Middleton, E.M., 2020. Fluorescence Correction Vegetation Index (FCVI): a physically based reflectance index to separate physiological and non-physiological information in far-red sun-induced chlorophyll fluorescence. Remote Sens. Environ. 240, 111676.
Yang, X., et al., 2015. Temperature dependence of an optical narrow-bandpass filter at 1.5 μm. Appl. Opt. 54 (1), 96–100.
Yang, X., et al., 2018c. FluoSpec 2—an automated field cpectroscopy system to monitor canopy solar-induced fluorescence. Sensors 18 (7), 2063.
Zarco-Tejada, P.J., et al., 2009. Imaging chlorophyll fluorescence with an airborne narrow-band multispectral camera for vegetation stress detection. Remote Sens. Environ. 113 (6), 1262–1275.
Zarco-Tejada, P.J., et al., 2018. Previsual symptoms of Xylella fastidiosa infection revealed in spectral plant-trait alterations. Nat.Plants 4 (7), 432–439.
Zeng, Y., Badgley, G., Dechant, B., Ryu, Y., Chen, M., Berry, J.A., 2019. A practical approach for estimating the escape ratio of near-infrared solar-induced chlorophyll fluorescence. Remote Sens. Environ. 232, 111209.
Zeng, Y., et al., 2022. Combining near-infrared radiance of vegetation and fluorescence spectroscopy to detect effects of abiotic changes and stresses. Remote Sens. Environ. 270, 112856.
Zhang, J.X., Hoshino, K., 2019. Optical transducers: optical molecular sensing and spectroscopy. Mol. Sensors Nanodevices 231–309.
Zhang, Y., et al., 2016. Consistency between sun-induced chlorophyll fluorescence and gross primary production of vegetation in North America. Remote Sens. Environ. 183, 154–169.
Zhou, X., Liu, Z., Xu, S., Zhang, W., Wu, J., 2016. An automated comparative observation system for sun-induced chlorophyll fluorescence of vegetation canopies. Sensors 16 (6), 775.
Zuromski, L.M., Bowling, D.R., Köhler, P., Frankenberg, C., Goulden, M.L., Blanken, P.D., Lin, J.C., 2018. Solar-induced fluorescence detects interannual variation in gross primary production of coniferous forests in the Western United States. Geophys. Res. Lett. 45 (14), 7184–7193.